

A sliding-window approach for latent restoring force modeling^{*}

Merijn Floren^{a,b,*}, Jan Swevers^{a,b}

^a*KU Leuven, Department of Mechanical Engineering, Leuven, 3001, Belgium*

^b*Flanders Make@KU Leuven, MPRO Core Lab, Leuven, 3001, Belgium*

ARTICLE INFO

Keywords:

Nonlinear system identification
Restoring force surface
Random-phase multisine excitation
State-space models
Best linear approximation

ABSTRACT

Restoring force surface (RFS) methods offer an attractive nonparametric framework for identifying nonlinear restoring forces directly from data, but their reliance on complete kinematic measurements at each degree of freedom limits scalability to multidimensional systems. The aim of this paper is to overcome these measurement limitations by proposing an identification framework with relaxed sensing requirements that exploits periodic multisine excitation. Starting from an initial linear model, a sliding-window feedback approach reconstructs latent states and nonlinear restoring forces nonparametrically, enabling identification of the nonlinear component through linear-in-parameters regression instead of highly non-convex optimization. Validation on synthetic and experimental datasets demonstrates high simulation accuracy and reliable recovery of physical parameters under partial sensing and noisy conditions.

1. Introduction

Identifying state-space models of mechanical systems from input-output data is inherently challenging, as the system dynamics depend on latent states that are not directly measurable. As a result, parameter estimation typically requires solving a highly nonlinear and non-convex optimization problem with an intrinsic recurrent structure imposed by the state evolution. However, this difficulty can be significantly alleviated if an estimate of the latent state trajectory can be obtained separately from the parameter estimation step. In that case, the recurrent nature of the identification problem effectively disappears, reducing parameter estimation to a considerably simpler regression problem.

The above procedure illustrates the fundamental rationale underlying restoring force surface (RFS) methods. As a concrete example, consider the single degree of freedom (SDOF) system studied in the original RFS formulation [12]:

$$m\ddot{y}(t) + f(y(t), \dot{y}(t)) = u(t), \quad (1)$$

where m denotes the mass, $y(t)$ the displacement, $u(t)$ the external excitation, and $f(\cdot)$ the total restoring force, representing the combined linear and nonlinear stiffness and damping forces acting on the system. In the original work [12], it is assumed that both the excitation $u(t)$ and the acceleration $\ddot{y}(t)$ are measured (or otherwise available), and that the mass m is known or can be reliably estimated. Under these assumptions, the restoring force can be isolated through simple algebraic rearrangement:

$$f(y(t), \dot{y}(t)) = u(t) - m\ddot{y}(t). \quad (2)$$

The right-hand side of (2) is therefore directly computable, enabling a fully nonparametric reconstruction of the restoring force behavior. The corresponding arguments of $f(\cdot)$ are obtained from the measured acceleration $\ddot{y}(t)$ through numerical integration, effectively reconstructing the latent states needed to avoid recursive parameter estimation. With these quantities available, the restoring force can be approximated using any suitable nonlinear function approximator¹. Crucially, this modeling step is performed in a static regression setting, where the restoring force is treated as an explicit algebraic mapping from $y(t)$ and $\dot{y}(t)$ to the computed force values, i.e., the right-hand side of (2). As a result, identifying $f(\cdot)$ reduces to a supervised function approximation problem with independent regression samples, rather than a recursive and non-convex dynamical estimation problem.

^{*}This work is supported by Flanders Make's IRVA projects ASSISStaNT and CoMoDO.

^{*}Corresponding author, e-mail: merijn.floren@kuleuven.be.

ORCID(s): 0000-0001-7265-7851 (M. Floren); 0000-0003-2034-5519 (J. Swevers)

¹The original study [12] employed polynomial basis functions, while later work also considered neural-network representations [13].

Although first introduced in 1979 [12], RFS methods remain relevant today; the survey in [15] recognizes them as a major time-domain identification technique, valued for their simplicity and intuitive, visual interpretations. RFS methods have, for example, been used to characterize the complex nonlinear forces at the wing-to-payload mounting interface in an F-16 fighter jet [3]. Other applications include predicting the response of elastomer materials [19], analyzing the variable stiffness of an elastomagnetic suspension [1], and identifying nonlinear behavior in a robotic arm [6].

1.1. Limitations of classical RFS methods

Despite its success, the original RFS method exhibits several limitations. First, it relies on knowledge of acceleration, velocity, and displacement. Ideally, all three quantities should be measured directly; however, this is often impractical or prohibitively expensive. In most applications, only one quantity is measured, while the remaining variables are obtained through numerical processing, a procedure that can introduce significant errors [22]. In mechanical systems, acceleration is typically measured, with velocity and displacement obtained via numerical integration. This procedure tends to amplify low-frequency noise and sensor drift over time, often requiring additional post-processing. Conversely, if displacement is measured, velocity and acceleration must be obtained through numerical differentiation, which rapidly becomes unreliable in the presence of measurement noise. A detailed discussion of the implications of numerical integration and differentiation for RFS-based approaches can be found in [22].

A second limitation of RFS methods arises from their demanding measurement requirements in higher-dimensional systems. Specifically, extending the SDOF restoring-force isolation in (2) to the multi degree of freedom (MDOF) case requires measurements at every degree of freedom [11, 14]. In practice, for high-dimensional systems, instrumenting all degrees of freedom quickly becomes impractical, as sensors may alter system dynamics, compromise structural integrity, be physically inaccessible, or result in excessive costs.

Although numerical post-processing and increased sensor coverage can partially alleviate these limitations, they do not fundamentally remove the strict measurement dependence of RFS methods. Recent work has therefore sought to address this issue more directly. In [18], a Bayesian formulation is proposed in which a linear system of ordinary differential equations (ODEs) is driven by a Gaussian process in time representing the unknown nonlinear component of the restoring force, enabling joint inference of both the latent state trajectory and the nonlinear restoring force. A related deterministic method was introduced in [5], where the nonlinear restoring force time series is analytically reconstructed from an initially fitted linear model using a sliding-window procedure. Both approaches, however, explicitly assume an SDOF system formulation and therefore do not extend directly to the MDOF setting.

1.2. Proposed approach

This work extends the rationale introduced in [5] to the MDOF setting, thereby substantially relaxing the measurement requirements of RFS methods in higher-dimensional systems. In particular, no restrictions are imposed on the type of measured quantity (displacement, velocity, or acceleration), nor on the number or spatial locations of the measured degrees of freedom². Following [5], the only requirement is that the system is excited using random-phase multisine signals, which enable estimation of the *best linear approximation* (BLA) from frequency response measurements [16]. This initial linear model is subsequently employed within a sliding-window framework to analytically reconstruct both the nonlinear restoring force and the associated latent state trajectory in the time domain. While the spatial location of the nonlinear restoring force is assumed to be known, its functional form and magnitude remain unknown. The linear dynamics are assumed to follow a known ODE structure, whereas the physical parameters of this linear subsystem are only approximately known through available initial estimates. The objective is twofold: to recover the true physical parameters of the underlying linear system and to obtain an accurate nonlinear model suitable for simulation and control applications.

1.3. Notation

The sets of real, integer, and natural numbers are denoted by \mathbb{R} , \mathbb{Z} , and \mathbb{N} , respectively. The identity matrix is denoted by I , and 0 denotes the zero matrix, with dimensions clear from context. For a real-valued vector $x \in \mathbb{R}^n$ and a symmetric positive definite matrix $Q \in \mathbb{R}^{n \times n}$, the squared weighted 2-norm is defined as $\|x\|_Q^2 = x^T Q x$, where x^T denotes the transpose of x . When a unit weighting is used, the notation simplifies to $\|x\|^2 = x^T x$. For complex-valued vectors, the same definition applies except that the Hermitian transpose, denoted by x^H , replaces the regular transpose. The imaginary unit is denoted by j . The exponential of a square matrix A is written as $\exp(A)$.

²Provided that the measured responses are dynamically coupled to the applied excitation.

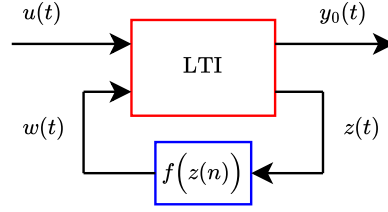


Figure 1: The *nonlinear linear fractional representation* (NL-LFR) model structure as a feedback interconnection of a linear time-invariant (LTI) system and a static nonlinear mapping.

1.4. Paper outline

The remainder of this paper is structured as follows. Section 2 defines the problem statement, after which Section 3 details the proposed sequential identification procedure. The methodology is validated using three case studies: a simulated SDOF system in Section 4.1, a simulated MDOF system with unmeasured nonlinear locations in Section 4.2, and experimental validation on an SDOF benchmark setup in Section 5. Conclusions are drawn in Section 6.

2. Problem statement

We consider the *periodic in, same period out* (PISPO) system class, comprising systems for which a periodic input yields a steady-state output with the same period³. The governing ODEs are assumed to follow a known structural form, with the exception of an unknown nonlinear restoring force, and are represented within the *nonlinear linear fractional representation* (NL-LFR) framework, in which nonlinear systems are described as a feedback interconnection between a linear time-invariant (LTI) dynamical system and a static nonlinear mapping, as illustrated in Fig. 1. The corresponding continuous-time system dynamics are described by the following state-space equations:

$$\dot{x}(t) = \mathcal{A}x(t) + \mathcal{B}_u u(t) + \mathcal{B}_w w(t), \quad (3a)$$

$$y_0(t) = \mathcal{C}_y x(t) + \mathcal{D}_{yu} u(t) + \mathcal{D}_{yw} w(t), \quad (3b)$$

$$z(t) = \mathcal{C}_z x(t), \quad (3c)$$

$$w(t) = f(z(t)), \quad (3d)$$

where $x(t) \in \mathbb{R}^{n_x}$ is the latent state, $u(t) \in \mathbb{R}^{n_u}$ the external input, $w(t) \in \mathbb{R}^{n_w}$ the nonlinear feedback input⁴, $y_0(t) \in \mathbb{R}^{n_y}$ the exact output, and $z(t) \in \mathbb{R}^{n_z}$ the latent argument of the nonlinear mapping $f : \mathbb{R}^{n_z} \rightarrow \mathbb{R}^{n_w}$. The matrices $\mathcal{A} \in \mathbb{R}^{n_x \times n_x}$, $\mathcal{B}_u \in \mathbb{R}^{n_x \times n_u}$, $\mathcal{B}_w \in \mathbb{R}^{n_x \times n_w}$, $\mathcal{C}_y \in \mathbb{R}^{n_y \times n_x}$, $\mathcal{C}_z \in \mathbb{R}^{n_z \times n_x}$, $\mathcal{D}_{yu} \in \mathbb{R}^{n_y \times n_u}$, and $\mathcal{D}_{yw} \in \mathbb{R}^{n_y \times n_w}$ describe the linear dynamics and input-output relationships. Since the linear system of ODEs is known, the structure of these matrices is also known. However, the values of the corresponding physical parameters θ_{phys} remain unknown, although an initial guess is available, denoted as $\theta_{\text{phys},0}$. The true parameters θ_{phys} correspond to the *underlying linear system*, which exclusively captures all linear input-output dynamics. Accordingly, the nonlinear mapping $f(\cdot)$ in (3d) is purely nonlinear⁵.

Data are collected from (3) by exciting the system with random-phase multisine inputs [16]:

$$u(n) := \frac{2}{\sqrt{N}} \sum_{k=1}^{N/2-1} U_k \cos(2\pi k f_0 n + \varphi_k), \quad (4)$$

where U_k denotes the excitation amplitude at frequency index k , and $f_0 = f_s/N$ is the frequency resolution, with f_s denoting the sampling frequency and N the (even) number of samples per period. The corresponding frequency of the k th harmonic is given by $f_k = k f_0$. The phases φ_k are independent and uniformly distributed over the interval $[0, 2\pi)$.

³The PISPO class encompasses a broad range of systems, including those exhibiting amplitude-dependent resonance and nonlinearities such as saturation and dead zones, while excluding phenomena that produce subharmonics, such as bifurcations and chaotic behavior.

⁴That is, the nonlinear restoring force.

⁵For instance, $f(z)$ cannot be expressed as $f(z) = Kz + g(z)$, where K is a constant matrix and $g(\cdot)$ is a nonlinear function.

Assumption 1. The input signal $u(n)$ is persistently exciting of sufficiently high order, such that all relevant system dynamics are excited over the frequency band of interest.

Assumption 2. The discrete-time signal (4) is applied to the continuous-time system (3) via zero-order hold (ZOH), i.e., $u_{\text{ZOH}}(t) := u(n)$, for $t \in [nT_s, (n+1)T_s)$, where $T_s = 1/f_s$ denotes the sampling period.

Assumption 3. The measured output is corrupted by additive, zero-mean, stationary noise $v(n)$ with finite variance, i.e., $y(n) := y_0(n) + v(n)$. The noise may be colored and is uncorrelated with the input $u(n)$, which is exactly known.

The resulting input-output dataset for parameter estimation consists of $P \geq 1$ steady-state periods of $R \geq n_u$ realizations of a random-phase multisine (4):

$$\mathcal{D} = \left\{ \left(u^{[r,p]}(n), y^{[r,p]}(n) \right) \right\}_{n=0, r=0, p=0}^{N-1, R-1, P-1}, \quad (5)$$

where both the input and output signals are zero-mean. Based on \mathcal{D} , the objective is to identify a discrete-time NL-LFR state-space model of the form:

$$x(n+1) = Ax(n) + B_u u(n) + B_w w(n), \quad (6a)$$

$$y(n) = C_y x(n) + D_{yu} u(n) + D_{yw} w(n), \quad (6b)$$

$$z(n) = C_z x(n), \quad (6c)$$

$$w(n) = \beta^T \phi(z(n)), \quad (6d)$$

where the discrete-time matrices in (6a) are related to their continuous-time counterparts in (3a) through the ZOH discretizations:

$$A = \exp(\mathcal{A}T_s), \quad B_u = \int_0^{T_s} \exp(\mathcal{A}\tau) \mathcal{B}_u d\tau, \quad B_w = \int_0^{T_s} \exp(\mathcal{A}\tau) \mathcal{B}_w d\tau, \quad (7)$$

while $C_y = C_y$, $C_z = C_z$, $D_{yu} = D_{yu}$, and $D_{yw} = D_{yw}$. Moreover, $\phi : \mathbb{R}^{n_z} \rightarrow \mathbb{R}^{n_\phi}$ represents a polynomial feature mapping with $\beta \in \mathbb{R}^{n_\phi \times n_w}$ the corresponding coefficient matrix. Optimization is thus carried out over the decision variables $\theta = (\theta_{\text{phys}}, \beta)$, which preserves the physical interpretability of the underlying linear system, despite the final model being expressed in discrete time. An implication of this choice is that the discrete-time matrices have to be recomputed at each iteration of the optimization routine that updates θ_{phys} . Fortunately, this can be done efficiently using a single matrix exponential [20]:

$$\begin{bmatrix} A & B \\ 0 & I \end{bmatrix} = \exp \left(\begin{bmatrix} \mathcal{A} & \mathcal{B} \\ 0 & 0 \end{bmatrix} T_s \right), \quad (8)$$

where $\mathcal{B} = [\mathcal{B}_u \ \mathcal{B}_w]$ and $B = [B_u \ B_w]$. In the remainder of this paper, all discrete-time matrices are obtained explicitly via this formulation.

Remark 1. The ZOH discretization method in (7) assumes that both inputs $u(t)$ and $w(t)$ are piecewise constant over each sampling interval $t \in [nT_s, (n+1)T_s)$ for all n . Under ideal experimental conditions, this assumption holds for the external excitation $u(t)$, but not for the internal feedback signal $w(t)$, which varies continuously. Consequently, the sampled continuous-time NL-LFR system in (3) cannot be represented exactly by the discrete-time model in (6). Nevertheless, by choosing a sufficiently small sampling period T_s , the induced approximation error can be kept within acceptable bounds.

3. A step-wise identification algorithm

A three-step identification algorithm is proposed. First, in Section 3.1, the initial physical parameters θ_{phys} are optimized to accurately capture the linearized input-output behavior. Second, in Section 3.2, the nonlinear restoring force is inferred nonparametrically, after which the parameters β are obtained by solving a linear system of equations, while keeping θ_{phys} fixed. Third, in Section 3.3, all parameters θ are jointly optimized to compensate for bias introduced in the preceding steps and to further improve the model's simulation accuracy.

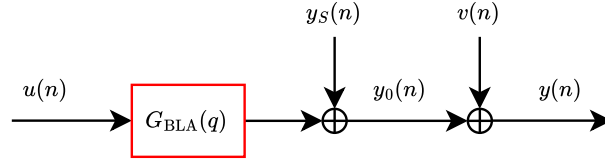


Figure 2: Schematic overview of the BLA framework. For random excitation signals with a Gaussian distribution, the response of a nonlinear system is replaced by the sum of an LTI approximation $G_{\text{BLA}}(q)$, unmodeled nonlinear dynamics $y_S(n)$, and a disturbing noise source $v(n)$.

3.1. Initial linear model

The PISPO system class and the assumed experimental conditions in Section 2 allow us to use the theory of the BLA [16, 4]. When applied with random excitation signals that follow a Gaussian distribution, such as the random-phase multisine (4), this framework represents the response of a nonlinear dynamical system as the sum of an LTI approximation, unmodeled nonlinear dynamics, and a disturbing noise source. A schematic representation of this concept is provided in Fig. 2. The BLA itself describes a linearized dynamic relationship between the zero-mean input $u(n)$ and the zero-mean output $y(n)$ that is optimal in the mean-square sense:

$$G_{\text{BLA}}(q) := \arg \min_G \mathbb{E} \left[\|y(n) - G(q)u(n)\|^2 \right], \quad (9)$$

where $\mathbb{E}[\cdot]$ denotes the expectation operator and q the forward-shift operator. As shown in [16], for the single-input case and under multisine excitation, the minimizer of (9) is equivalent to

$$G_{\text{BLA}}(j\omega_k) = \mathbb{E} \left[\frac{Y(k)}{U(k)} \right], \quad (10)$$

where $Y(k)$ and $U(k)$ denote the leakage-free discrete Fourier transforms (DFTs) of $y(n)$ and $u(n)$, respectively, at frequency line k , therefore $\omega_k = 2\pi k f_0$. The expectation is taken over different periods and realizations in \mathcal{D} .

In our setting, the nonparametric BLA provides an averaged frequency response matrix (FRM) that facilitates the subsequent parametrization of the model components directly related to the NL-LFR input-output behavior, i.e., the state-space matrices \mathcal{A} , \mathcal{B}_u , \mathcal{C}_y , and \mathcal{D}_{yu} . Furthermore, the BLA estimation procedure yields an assessment of the nonlinear distortions and the disturbing noise level, offering valuable insight into the system's behavior. These quantities can also be incorporated into the parameter estimation procedure as weighting functions. For more details on the BLA estimation procedure and its properties, we refer to [16, 4].

Let $\hat{G}_{\text{BLA}}(j\omega_k)$ denote the nonparametric estimate of the BLA at frequency ω_k . The corresponding parametric BLA, parametrized by θ_{phys} , is given by

$$G(\zeta_k | \theta_{\text{phys}}) = C_y(\zeta_k I - A)^{-1} B_u + D_{yu}, \quad (11)$$

where ζ_k denotes the z-transform variable evaluated on the unit circle at frequency $f_k = k f_0$. Starting from the initial guess $\theta_{\text{phys},0}$, the physical parameters θ_{phys} are optimized by minimizing the weighted squared residuals between the nonparametric and parametric BLA estimates over the excited frequency lines:

$$\underset{\theta_{\text{phys}}}{\text{minimize}} \quad \frac{1}{|\mathcal{K}|} \sum_{k \in \mathcal{K}} \left\| W(k) \odot (\hat{G}_{\text{BLA}}(j\omega_k) - G(\zeta_k | \theta_{\text{phys}})) \right\|_F^2, \quad (12)$$

where $\|\cdot\|_F^2$ represents the squared Frobenius norm, \odot the element-wise Hadamard product, and $\mathcal{K} \subseteq \{1, \dots, N/2-1\}$ the set of excited frequency lines, with $|\mathcal{K}|$ denoting its cardinality. Moreover, $W(k)$ denotes a frequency-dependent weighting matrix, which, in principle, can be any well-chosen real-valued matrix. Yet, we adopt the common choice of weighting the squared model residuals by the reciprocal of the total variance of the nonparametric BLA estimates (see [16, Ch. 4.3.1]). Such weighting effectively implements a whitening transformation that accounts for unequal variance for unequal variance across frequency lines. If the total variance estimate is not available, i.e., in case of a single multisine experiment, a unity weighting is applied instead.

Remark 2. In the parametrization of the BLA in (12), each excited frequency line is treated independently within the optimization problem. This decoupling eliminates the recursion-induced non-convexity typically encountered in time-domain parameter estimation, leading to a substantially more tractable optimization problem.

Remark 3. The nonparametric BLA is affected by a systematic error due to nonlinear distortions [16]. Consequently, the nonparametric BLA is biased, and optimizing θ_{phys} by minimizing the model residual in (12) results in biased parameter estimates. This bias conflicts with the objective of identifying the true physical parameters. Nevertheless, at this stage, the primary objective is to achieve accurate simulation performance. The resulting bias will be addressed and compensated for in the final step of the proposed algorithm, described in Section 3.3.

3.2. Modeling the nonlinear restoring force

In this second step, the nonlinear restoring force and the latent state trajectories are identified for fixed θ_{phys} . To improve both the signal-to-noise ratio (SNR) and the computational efficiency we proceed with the sample means $u^{[r]}(n) = \frac{1}{P} \sum_{p=0}^{P-1} u^{[r,p]}(n)$ and $y^{[r]}(n) = \frac{1}{P} \sum_{p=0}^{P-1} y^{[r,p]}(n)$. Note that under the ZOH assumption, averaging over the inputs is redundant as they are noise-free, i.e., $u^{[r]}(n) = u^{[r,p]}(n)$. Nevertheless, we include this step here to accommodate the case where measured (and thus noisy) input data are used instead.

3.2.1. A nonparametric sliding window feedback approach

When simulating the output of the parametric BLA model and comparing it to the measured output, a mismatch arises due to the unmodeled nonlinear dynamics. The idea of this step is to obtain a nonparametric estimate of the nonlinear feedback force w that improves the agreement between the simulated and measured outputs. To this end, we propose a sliding window strategy, in which the nonlinear feedback force is estimated by solving a local optimization problem over a finite time horizon that is shifted forward at each sample instant. Specifically, the nonlinear feedback force is estimated over a window of length $H + 1 \ll N$, with $H \in \mathbb{N}$ being the prediction horizon length. Only the solution corresponding to the current time instance is retained and used to shift the window forward in time by one sample. This procedure is repeated until all N time steps have been processed. Along the way, the full latent state x is naturally inferred as well.

We first define the stacked vectors:

$$\mathcal{U}^{[r]}(n) = \begin{bmatrix} u^{[r]}(n) \\ u^{[r]}(n+1) \\ \vdots \\ u^{[r]}(n+H) \end{bmatrix}, \quad \mathcal{Y}^{[r]}(n) = \begin{bmatrix} y^{[r]}(n) \\ y^{[r]}(n+1) \\ \vdots \\ y^{[r]}(n+H) \end{bmatrix}, \quad \mathcal{W}^{[r]}(n) = \begin{bmatrix} w^{[r]}(n) \\ w^{[r]}(n+1) \\ \vdots \\ w^{[r]}(n+H) \end{bmatrix}, \quad (13)$$

with dimensions $\mathbb{R}^{(H+1)n_u}$, $\mathbb{R}^{(H+1)n_y}$, and $\mathbb{R}^{(H+1)n_w}$, respectively. Then, the optimization problem that is solved for each time step $n \in \{0, \dots, N-1\}$ and each realization $r \in \{0, \dots, R-1\}$ is given by

$$\underset{\mathcal{W}^{[r]}(n)}{\text{minimize}} \quad \frac{1}{2} \left\| \mathcal{Y}^{[r]}(n) - \hat{\mathcal{Y}}^{[r]}(n) \right\|_{\mathcal{Q}}^2 + \frac{\lambda}{2} \left\| \mathcal{W}^{[r]}(n) \right\|^2, \quad (14a)$$

$$\text{subject to} \quad \hat{\mathcal{Y}}^{[r]}(n) = \mathcal{O}_x x_*^{[r]}(n) + S_u \mathcal{U}^{[r]}(n) + S_w \mathcal{W}^{[r]}(n), \quad (14b)$$

where $\lambda \in \mathbb{R}_{>0}$ is a regularization parameter that controls the solution variability, and \mathcal{Q} is a block-diagonal matrix formed by concatenating $H + 1$ copies of the inverse of the time-domain sample noise covariance matrix defined in (29)⁶. Equation (14b) expresses the stacked simulated output as a function of the initial state $x_*^{[r]}(n)$, which will be defined shortly, and the stacked inputs $\mathcal{U}^{[r]}(n)$ and $\mathcal{W}^{[r]}(n)$; the evolution of this sequence is described with the following block-matrices:

$$\mathcal{O}_x = \begin{bmatrix} C_y \\ C_y A \\ \vdots \\ C_y A^H \end{bmatrix}, \quad S_u = \begin{bmatrix} D_{yu} & 0 & \dots & 0 \\ C_y B_u & D_{yu} & \dots & 0 \\ \vdots & \vdots & \ddots & \vdots \\ C_y A^{H-1} B_u & C_y A^{H-2} B_u & \dots & D_{yu} \end{bmatrix}, \quad S_w = \begin{bmatrix} D_{yw} & 0 & \dots & 0 \\ C_y B_w & D_{yw} & \dots & 0 \\ \vdots & \vdots & \ddots & \vdots \\ C_y A^{H-1} B_w & C_y A^{H-2} B_w & \dots & D_{yw} \end{bmatrix}, \quad (15)$$

⁶In cases where the sample noise covariance matrix is not available, \mathcal{Q} is constructed as a diagonal matrix containing the inverses of the output variances. Doing so ensures that, in the multi-output case, the different outputs are properly scaled relative to their magnitudes.

with dimensions $\mathbb{R}^{n_y(H+1) \times n_x}$, $\mathbb{R}^{n_y(H+1) \times n_u(H+1)}$, and $\mathbb{R}^{n_y(H+1) \times n_w(H+1)}$, respectively.

The optimization problem in (14) is convex. Therefore, by substituting (14b) into (14a), setting the gradient with respect to $\mathcal{W}^{[r]}(n)$ to zero, and solving for $\mathcal{W}^{[r]}(n)$, we obtain the closed-form solution:

$$\mathcal{W}_*^{[r]}(n) = -\mathcal{G}^{-1} S_w^T Q (\mathcal{O}_x x_*^{[r]}(n) + S_u \mathcal{U}^{[r]}(n) - \mathcal{Y}^{[r]}(n)), \quad (16)$$

where $\mathcal{G} = S_w^T Q S_w + \lambda I$.

Remark 4. The regularization term in (14a) is introduced to address two practical issues. First, the measured output data $\mathcal{Y}^{[r]}(n)$ are corrupted by noise, and without regularization (i.e., when $\lambda = 0$) the minimizer of (14) would be highly sensitive to this noise, resulting in large variability in the inferred $\mathcal{W}_*^{[r]}(n)$. Second, when $n_w > n_y$, the unregularized optimization problem is inherently ill-posed (i.e., \mathcal{G} is rank-deficient), leading to non-unique solutions; the regularization term in (14a) ensures that a unique minimizer exists in such cases. The hyperparameter λ controls the trade-off between data fit and solution variability.

Remark 5. The main motivation for using a prediction horizon length greater than one, or a longer window in general, lies in its ability to mitigate the effects of measurement noise. When the window is short, $\mathcal{W}_*^{[r]}(n)$ may become overly sensitive to high-frequency noise in $\mathcal{Y}^{[r]}(n)$, thus resulting in a nervous estimate. In contrast, longer windows naturally lead to smoother solutions, as the individual noisy samples are averaged out over time. The effect of the prediction horizon length H and regularization parameter λ , including their sensitivity to different noise levels, is empirically studied in Section 4.

Equation (16) provides the optimal solution over the defined window, and is naturally defined for all R realizations provided that $n < N - H$. That is, when $n \geq N - H$, computing $\mathcal{U}^{[r]}(n)$ and $\mathcal{Y}^{[r]}(n)$ requires “future” input-output data beyond the final sample instant. However, thanks to periodicity, we are able to define the input-output data at every possible time step $m \in \mathbb{Z}$ in terms of the first N samples as follows:

$$u^{[r]}(m) := u^{[r]}(m \bmod N), \quad y^{[r]}(m) := y^{[r]}(m \bmod N), \quad (17)$$

where mod denotes the modulus operator. Using (17), the optimal solution in (16) is well-defined at each time step and for every realization. However, in (16), the initial state of each window, denoted $x_*^{[r]}(n)$, is required. The recursive evolution of this state gives rise to the “sliding” nature of the proposed approach, as detailed next.

To advance to the next sample, we only use the first n_w elements of $\mathcal{W}_*^{[r]}(n)$, which we denote with $w_*^{[r]}(n)$. These elements correspond to the current time step, and are related to the state according to

$$x_*^{[r]}(n) = \begin{cases} x_0^{[r]}, & \text{if } n = 0 \\ A x_*^{[r]}(n-1) + B_u u^{[r]}(n-1) + B_w w_*^{[r]}(n-1), & \text{otherwise} \end{cases}, \quad (18)$$

which shows that a value for $x_0^{[r]}$ is still needed at $n = 0$. This initial state is typically unknown, and arbitrarily setting it (e.g., to zero) introduces a transient response that is incompatible with the true system, and, therefore, unsuitable for parametric modeling of the nonlinear restoring force. While simply discarding the corresponding transient samples is possible, it also results in the loss of valuable information.

Instead, the idea is to use the parametric BLA model to obtain a more informed initial state. In addition, the periodicity definition in (17) can be leveraged to retain all N samples. Specifically, the BLA state trajectories are computed in the frequency domain as

$$X_{\text{BLA}}^{[r]}(k) = (\zeta_k I - A)^{-1} B_u \mathcal{U}^{[r]}(k), \quad (19)$$

where $\mathcal{U}^{[r]}(k)$ denotes the DFT of $u^{[r]}(n)$ at frequency line k . Taking the inverse DFT (IDFT) of $X_{\text{BLA}}^{[r]}(k)$ yields $x_{\text{BLA}}^{[r]}(m) := x_{\text{BLA}}^{[r]}(m \bmod N)$ for $m \in \mathbb{Z}$. This periodicity is essential, as it allows the simulation to be initialized at an arbitrary phase of the same periodic trajectory. Concretely, in (18) we define $x_0^{[r]} := x_{\text{BLA}}^{[r]}(-N_0)$ and $u^{[r]}(0) := u^{[r]}(-N_0)$, where $N_0 \in \mathbb{N}_0$ denotes the number of offset samples required for the transient to decay. The simulation is then run for a total of $N + N_0$ samples, after which the first N_0 samples of the resulting sequences are discarded.

In summary, the proposed procedure described in this section yields an analytical expression for the missing nonlinear restoring force, which can be evaluated efficiently over the entire time series. For given values of the horizon length H , regularization strength λ , and offset length N_0 , advancing the simulation one sample at a time yields a set of paired samples as

$$\mathcal{D}_{wz} = \left\{ \left(w_*^{[r]}(n), z_*^{[r]}(n) \right) \right\}_{n=0, r=0}^{N-1, R-1}, \quad (20)$$

where $z_*^{[r]}(n)$ is easily derived from $x_*^{[r]}(n)$ through (6c). This dataset will be used in the next step for parametric modeling of the nonlinear restoring force.

3.2.2. Parametric modeling of the nonlinear restoring force

Given \mathcal{D}_{wz} , estimating the nonlinear coefficient matrix β reduces to solving a set of linear regression problems. Due to the black-box nature of the polynomial basis function model, the individual entries of β do not necessarily carry a direct physical interpretation. Nevertheless, when $n_w > 1$, it is important that β respects the physical location of the nonlinearities.

To enforce this structure, we introduce a binary selection matrix $P_{z,i} \in \{0, 1\}^{n_{z,i} \times n_z}$, which, for each location $i \in \{1, \dots, n_w\}$, extracts the correct subvector of dimension $n_{z,i} \leq n_z$ from z . The corresponding nonlinear restoring force term is then modeled as

$$w_i(n) = \beta_i^T \phi_i(P_{z,i} z(n)), \quad (21)$$

where $\phi_i : \mathbb{R}^{n_{z,i}} \rightarrow \mathbb{R}^{n_{\phi,i}}$ is a monomial feature map, and $\beta_i \in \mathbb{R}^{n_{\phi,i}}$ contains the associated coefficients.

The full nonlinear mapping in (6d) is subsequently defined as a decoupled combination of the individual nonlinearities through

$$\beta := \begin{bmatrix} \beta_1 & \dots & 0 \\ \vdots & \ddots & \vdots \\ 0 & \dots & \beta_{n_w} \end{bmatrix} \in \mathbb{R}^{n_{\phi} \times n_w}, \quad \phi := \begin{bmatrix} \phi_1 \\ \vdots \\ \phi_{n_w} \end{bmatrix} : \mathbb{R}^{n_z} \rightarrow \mathbb{R}^{n_{\phi}}, \quad (22)$$

with $n_{\phi} = \sum_{i=1}^{n_w} n_{\phi,i}$. Since (21) is linear in the unknown parameters, each vector β_i can be estimated analytically using ordinary least squares on the input-target pairs from \mathcal{D}_{wz} , aggregated over all R realizations. Doing so yields the estimated nonlinear coefficient matrix β , which, together with θ_{phys} , fully initializes the NL-LFR model.

Remark 6. The bias in the θ_{phys} estimate has an important impact on the structure of the monomials in $\phi_i(\cdot)$. Specifically, the restoring force estimates w_* inferred through (14) absorb the discrepancy between the true linear state trajectories and those reconstructed using the estimated linear parameters. As a result, the inferred force contains an additional component that depends approximately linearly on the reconstructed state trajectories. Consequently, $\phi_i(\cdot)$ must include degree-one monomials to accurately represent the mapping from z_* to w_* , even though the true restoring force in (3d) corresponds to a purely nonlinear mapping in z . This discrepancy motivates the bias-correction procedure and enables recovery of the true linear parameters in the subsequent step.

3.3. Final optimization

The previous steps provided fully initialized estimates of the parameters $\theta = (\theta_{\text{phys}}, \beta)$. In this final step, the goal is twofold: (i) to enhance the simulation performance and (ii) to recover the true system parameters. These objectives are addressed by solving the following optimization problem:

$$\underset{\theta}{\text{minimize}} \quad \frac{1}{RN} \sum_{r=0}^{R-1} \sum_{k=0}^{N/2} \|Y^{[r]}(k) - \hat{Y}^{[r]}(k | \theta)\|_{W(k)}^2 + \gamma \|\beta^{[1]}(\theta)\|_1. \quad (23)$$

The first component in (23) quantifies the simulation error in the frequency domain. Here, $Y^{[r]}(k)$ is the measured output spectrum, computed by applying the DFT to $y^{[r]}(n)$, while $\hat{Y}^{[r]}(k | \theta)$ is the modeled output spectrum, obtained by simulating the NL-LFR model in (6) with input $u^{[r]}(n)$ and then applying the DFT to the resulting time-domain output. To avoid spectral leakage caused by transients from an unknown initial state, we implement the same procedure described in Section 3.2.1, i.e., simulating and subsequently discarding N_0 offset samples to ensure steady-state

conditions. The proposed frequency-domain evaluation allows the weighting matrix $W(k)$ to account for the varying noise characteristics across frequencies. When available, the inverse of the sample noise covariance matrix in (30) is used at each frequency line. If this matrix is not available, $W(k)$ is instead constructed as a diagonal matrix containing the inverses of the output variances at each frequency, ensuring that the samples are properly balanced both across frequencies and, in the multi-output case, across different outputs.

The second component in (23) serves as a regularization term aimed at recovering the true underlying linear parameters. As discussed in Remark 6, the initial estimates of both θ_{phys} and β include components associated with linear dynamics, which renders the former non-unique and therefore not physically interpretable. To address this ambiguity, the elements of β that correspond to first-degree monomials are stacked into vector $\beta^{[1]}(\theta)$ and penalized using the sparsity-promoting ℓ_1 -norm, denoted by $\|\cdot\|_1$. This strategy effectively redirects the contribution of $\beta^{[1]}(\theta)$ into θ_{phys} , thereby encouraging the recovery of the true physical values. The strength of the proposed regularization term is controlled through hyperparameter $\gamma \in \mathbb{R}_{\geq 0}$.

3.4. Implementation details

All algorithms are implemented in Python. The optimization routines are formulated using JAX [2] together with Equinox [7], enabling automatic differentiation and efficient execution on both CPUs and GPUs. Nonlinear least-squares problems are solved using the Levenberg-Marquardt algorithm [9, 10] as provided by the `Optimistic` library [17].

4. Simulation studies

Two simulation examples are presented to demonstrate the proposed step-wise algorithm. The first considers an SDOF Duffing oscillator and analyzes the influence of the different training steps, hyperparameters, and noise levels on model performance. The second examines a more complex MDOF system under limited sensing conditions.

4.1. SDOF Duffing oscillator

In this section we study in detail the proposed step-wise algorithm on a simulation example of a forced Duffing oscillator, of which the dynamics are described by the following ODE:

$$m\ddot{y}_0(t) + c\dot{y}_0(t) + ky_0(t) + k_3y_0^3(t) = u(t), \quad (24)$$

with m , c and k the linear mass, damping and stiffness parameters, respectively, and k_3 the cubic stiffness parameter. Here, the exact noise-free output $y_0(t)$ describes the displacement of the mass, while the input $u(t)$ acts as an external forcing term applied to the system. If we define $x(t) = [y_0(t), \dot{y}_0(t)]^T$, the Duffing dynamics in (24) adhere to the NL-LFR structure of (3), with

$$\begin{aligned} A &= \begin{bmatrix} 0 & 1 \\ -k/m & -c/m \end{bmatrix}, & B_u &= -B_w = \begin{bmatrix} 0 \\ 1/m \end{bmatrix}, \\ C_y &= C_z = [1 \quad 0], & D_{yu} &= D_{yw} = 0, \end{aligned} \quad (25)$$

and the typically unknown $f(z(t)) = k_3z^3(t)$. Within this formulation, the physical parameter vector is defined as $\theta_{\text{phys}} = (m, c, k)$.

We generate synthetic input-output data by solving the Duffing equation (24) using the fourth-order Runge-Kutta (RK4) integration scheme. The parameters of the Duffing oscillator are set to $m = 1$ kg, $c = 2$ N s m⁻¹, $k = 100$ N m⁻¹, and $k_3 = 500$ N m⁻³. The training data consists of $R = 5$ realizations of $P = 2$ steady-state periods of a random-phase multisine (4), with $N = 8192$ samples each. The multisine input signal excites frequencies up to 10 Hz, is sampled at $f_s = 128$ Hz, and has individual amplitudes U_k chosen such that an overall root mean square (RMS) amplitude of 12 N is obtained. Starting from noise-free samples, we generate three datasets with increasing output noise levels, ranging from almost noise-free to strongly corrupted. Specifically, white Gaussian noise is added to the noise-free data to achieve SNRs of 60 dB, 40 dB and 20 dB. From these SNRs, lower bounds on the achievable relative simulation errors can be derived, corresponding to 0.1 %, 1 % and 10 %, respectively⁷.

⁷These bounds follow directly from the definition $\text{SNR} = 10 \log_{10}(P_s/P_n)$, where P_s and P_n denote the signal and noise power, respectively. The lower bound is then defined as the noise-to-signal amplitude ratio, i.e. $\sqrt{P_n}/\sqrt{P_s} = 10^{-\text{SNR}/20}$, expressed as a percentage.

Table 1

Parameter estimates of the Duffing oscillator obtained using the BLA procedure for 100 different initializations in (26). The estimates (mean \pm standard deviation) are highly consistent across initializations and noise levels, but bias is present, most noticeable in the stiffness parameter k , which is systematically overestimated due to the hardening effect of the cubic spring.

	m [kg]	c [N s m ⁻¹]	k [N m ⁻¹]
true	1.00	2.00	100
SNR 60 dB	$0.988 \pm 5.77 \times 10^{-6}$	$2.10 \pm 6.34 \times 10^{-6}$	$114 \pm 6.44 \times 10^{-4}$
SNR 40 dB	$0.988 \pm 1.01 \times 10^{-5}$	$2.10 \pm 8.07 \times 10^{-6}$	$114 \pm 1.13 \times 10^{-3}$
SNR 20 dB	$0.987 \pm 1.53 \times 10^{-6}$	$2.10 \pm 5.77 \times 10^{-6}$	$114 \pm 1.76 \times 10^{-4}$

Table 2

Simulation output normalized root mean square errors (NRMSEs) for the Duffing oscillator at different stages of the step-wise algorithm; compared to their respective theoretical lower bounds. The initial NL-LFR models already show a significant improvement over the BLA; for SNRs of 60 dB and 40 dB, the lower bounds are not met, likely because the ZOH discretization error exceeds the respective noise levels.

	NRMSEs [%]			
	BLA	initial NL-LFR	optimized NL-LFR	lower bound
SNR 60 dB	20.5	4.38	1.08	0.10
SNR 40 dB	20.5	4.51	1.48	1.00
SNR 20 dB	22.8	10.8	10.0	10.0

The goal of this simulation example is threefold: first, to assess how each training step (BLA estimation, restoring force modeling, and final optimization) affects the parameter estimates and contributes to the model's simulation performance; second, to study the influence of the regularization strength λ and prediction horizon length H on the restoring force approach; and third, to evaluate the sensitivity of the above analyses with respect to the different levels of measurement noise.

Step I: Best linear approximation

The first step consists of estimating the parameters of the linear part of the model, as outlined in Section 3.1. The concrete outcome is a linearized state-space model with estimates of the parameters m , c , and k . To assess the sensitivity of the parameter estimates to initialization, we repeat the optimization procedure 100 times, each with a maximum of 100 Levenberg-Marquardt iterations, starting from different initial guesses generated as follows:

$$\begin{bmatrix} m_0 \\ c_0 \\ k_0 \end{bmatrix} = \begin{bmatrix} m(1 + \delta_m) \\ c(1 + \delta_c) \\ k(1 + \delta_k) \end{bmatrix}, \quad \text{where } \delta_m, \delta_c, \delta_k \sim \mathcal{U}(-0.9, 0.9), \quad (26)$$

with $\mathcal{U}(-0.9, 0.9)$ denoting independent random variables sampled from a uniform distribution over the interval $[-0.9, 0.9]$. In other words, each parameter is randomly initialized within $\pm 90\%$ of its true value.

The identification procedure was then carried out as described above, and the resulting parameter estimates are summarized in Table 1. Two main observations can be drawn from these results. First, the estimates are highly consistent across the 100 runs and noise levels, with small standard deviations indicating robust convergence to a unique solution. Second, the estimates are generally close to the true values, but a bias is present, as expected. This bias is most noticeable in the stiffness parameter k , which is systematically overestimated due to the hardening effect of the cubic stiffness term k_3 . For further analyses, we proceed with the mean values of the estimates in Table 1.

We assess the simulation performance of the obtained BLA model using the normalized RMS error (NRMSE), computed here on the output signal⁸. The results, shown in Table 2, indicate a consistent NRMSE of around 20% across all noise levels. This relatively high error confirms that the linear model fails to adequately capture the Duffing oscillator's nonlinear behavior.

⁸In general, the NRMSE is computed as the RMS value of the respective error signal divided by the RMS value of the reference signal, multiplied by 100%, thereby providing a relative and easily interpretable measure of performance.

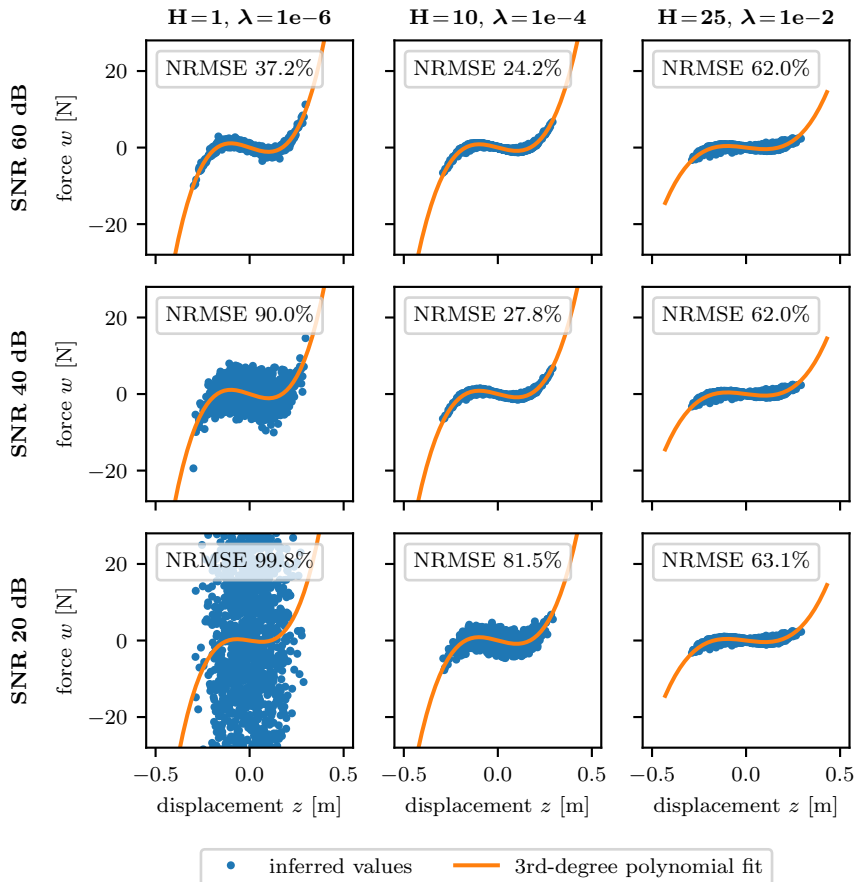


Figure 3: Visualization of D_{wz} and corresponding polynomial fit for three hyperparameter combinations across all noise levels. The inferred values, obtained by solving (14), generally suggest the correct cubic nature of the restoring force, but the influence of noise and hyperparameters is evident.

Step II: Restoring force modeling

In this second step, we address two main questions: (i) can the sliding-window approach suggest a restoring force *signal* that drives the simulated output close to the desired output, and (ii) can a static nonlinear *mapping* $f : \mathbb{R}^{n_z} \rightarrow \mathbb{R}^{n_w}$ be obtained from this signal? Particular attention is paid to the influence of the regularization parameter λ , the prediction horizon length H , and the impact of measurement noise on the results. In the following, the offset length is set to $N_0 = 100$ samples.

Figure 3 visualizes the inferred dataset D_{wz} (in blue) for three hyperparameter settings across all noise levels, where the nonparametric restoring force w is plotted as a function of the displacement z . Although not visible from the plots, in each case the inferred restoring force, obtained by solving (14), has successfully driven the simulated output close to the desired output. When plotted against displacement, this nonparametric force generally reveals the expected cubic nature of the underlying system nonlinearity. However, the corresponding third-degree odd polynomial⁹ fits (in orange) and their NRMSEs indicate that the relationship between z and w does not always reflect a clear static mapping. This phenomenon is most pronounced in the bottom-left plot, corresponding to the highest noise level combined with the shortest window length and weakest regularization. Here, the result lacks any meaningful structure, making it generally impossible to extract a reliable mapping from the signals in D_{wz} .

A more detailed analysis is carried out by performing a grid search over the hyperparameters. The prediction horizon length H is varied linearly from 1 to 50, while the regularization parameter λ is varied logarithmically from 10^{-7} to 10^{-1} , using 50 values in total. The results are summarized in Fig. 4, where the left column shows the

⁹Specifically, $\phi(z) = [z, z^3]^T$, as this structure matches the true underlying nonlinearity and includes the linear term required to compensate for the bias in the θ_{phys} estimate (see Remark 6).

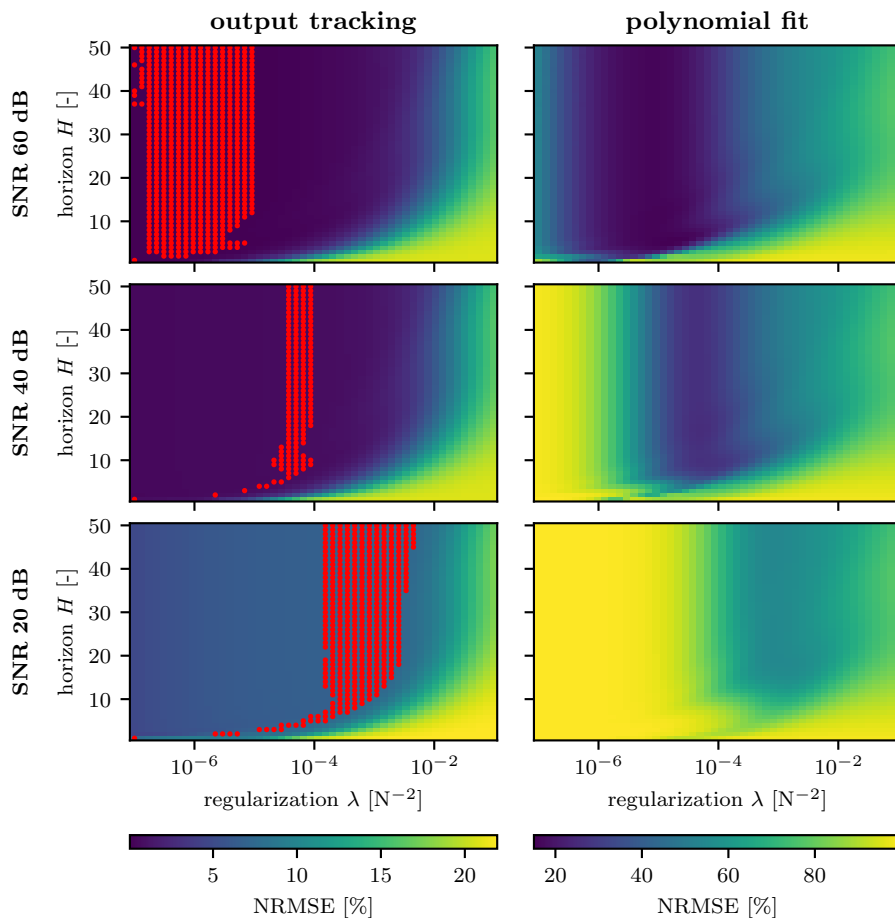


Figure 4: Grid search over the horizon length H and regularization strength λ . The left column shows nonparametric NRMSEs between measured and simulated output signals, while the right column shows parametric NRMSEs of the corresponding polynomial fits. Red dots mark hyperparameter combinations where the nonparametric NRMSEs are close to their lower bounds; these combinations also yield the most accurate polynomial fits.

nonparametric NRMSEs between the measured and simulated outputs, while the right column presents the NRMSEs of third-degree odd polynomial fits to the inferred restoring force signals, similar to Fig. 3. The red dots mark the hyperparameter combinations for which the nonparametric output NRMSEs are considered close¹⁰ to their lower bounds derived from the SNR. When examining λ first, Fig. 4 indicates that smaller values tend to reduce the nonparametric output NRMSE. However, this does not guarantee a good polynomial fit, since insufficient regularization causes the sliding-window algorithm to overfit the noise. The best polynomial fits are achieved at combinations that render the nonparametric output NRMSEs close to their respective lower bounds. Here, regularization suppresses noise just enough without being too restrictive. As for the prediction horizon length H , its effect is less pronounced, but it is clear that in general the window length should at least be a few samples long. Moreover, it can be observed that longer windows are preferred for higher noise levels. As discussed in Remark 5, this is because longer windows allow the algorithm to average out the high-frequency noise, leading to smoother estimates of the restoring force signal. Note that, in terms of computational cost, longer windows are somewhat more expensive to solve, but since the optimization problem admits an analytical solution, this increase is limited.

Finally, we assess the simulation performance of the initial NL-LFR models obtained from the hyperparameter combination $H = 10$ and $\lambda = 10^{-4}$, i.e., the second column in Fig. 3. The corresponding simulation output NRMSEs, presented in Table 2, show a performance gain of more than a factor of four for the SNRs of 60 dB and 40 dB, but further improvement is still required. At the SNR of 20 dB, the simulation accuracy is already close to the lower bound

¹⁰Defined using a relative tolerance of 5% and an absolute tolerance of 0.02%, with the larger of the two used as threshold.

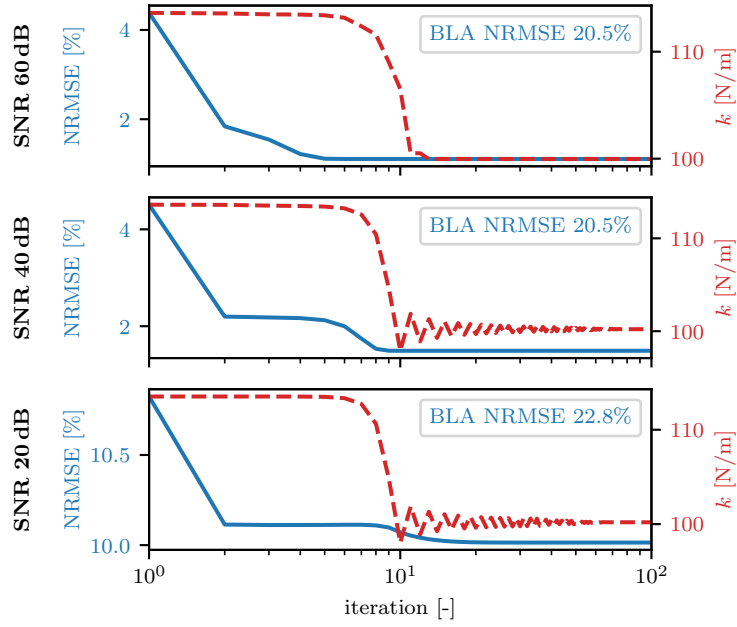


Figure 5: Evolution of the output simulation NRMSE and the linear stiffness parameter k over the iterations of the final optimization step. It can be seen that the optimization procedure first prioritizes reducing the simulation error, followed by correcting the bias in the stiffness parameter.

Table 3

Physical parameter estimates of the Duffing oscillator after the final optimization step. Compared with Table 1, the bias in the stiffness parameter is almost entirely eliminated.

	m [kg]	c [Ns m ⁻¹]	k [Nm ⁻¹]	k_3 [Nm ⁻³]
true	1.00	2.00	100	500
SNR 60 dB	0.999	2.06	99.9	485
SNR 40 dB	0.999	2.06	100	485
SNR 20 dB	0.999	2.06	100	487

of 10.0 %, despite the relatively large error observed in the polynomial fit of Fig. 3. This polynomial model nonetheless captured the key cubic trend of the restoring force, which proves sufficient for accurate simulation. We proceed with the above initial NL-LFR models to the next identification step.

Step III: Final optimization

The final identification step aims to improve the simulation performance of the initial NL-LFR models, while simultaneously recovering the true parameters of the Duffing oscillator. This goal is achieved by minimizing the dual-objective cost function in (23) using 100 Levenberg-Marquardt iterations with a regularization parameter of $\gamma = 5 \times 10^{-3}$. Figure 5 shows the evolution of the output NRMSEs and the stiffness parameter k over the iterations. It can be observed that the optimization procedure initially focuses on reducing the NRMSE, and subsequently on correcting the parameter bias. For all three SNRs, the NRMSE is significantly reduced, while the bias on k is almost entirely removed, as also apparent from the final parameter estimates in Table 3.

The final output NRMSEs in Table 2 confirm a substantial improvement in simulation performance. However, for SNRs of 60 dB and 40 dB, the NRMSEs remain above the ideal values expected from the noise levels. Since the model structure is correctly specified and noise is limited, this discrepancy is most plausibly due to the ZOH discretization, which does not exactly replicate the underlying continuous-time ODE, as discussed in Remark 1. This discretization mismatch may also explain why not all parameters in Table 3 are recovered exactly.

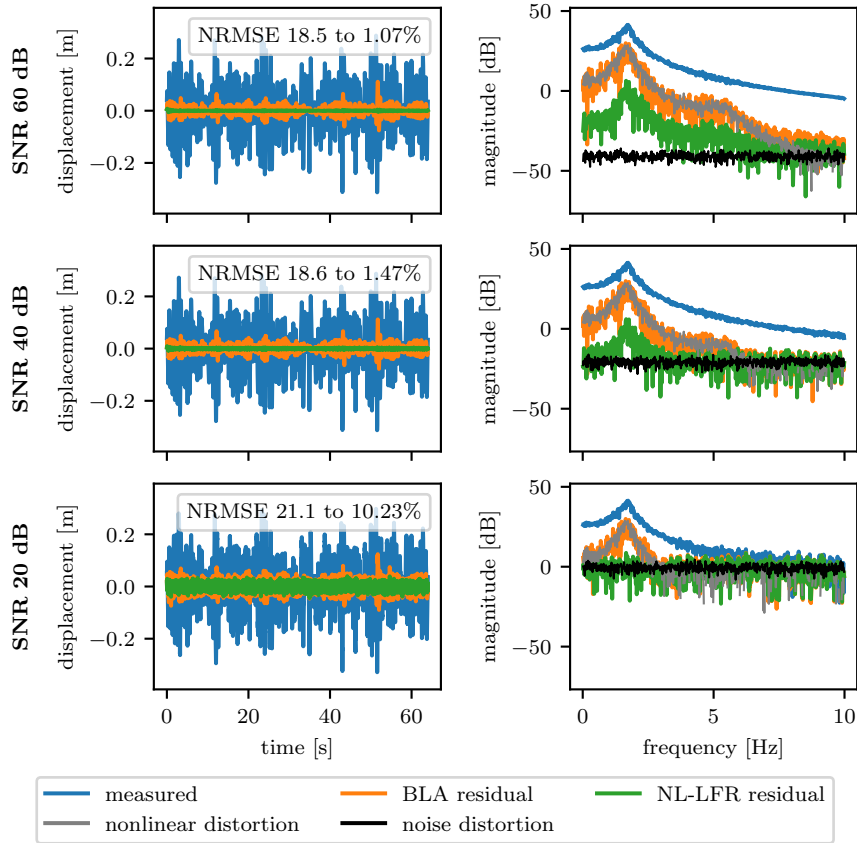


Figure 6: Test data: simulation performance of the Duffing oscillator BLA and NL-LFR models in time and frequency domains across different noise levels. Although the NL-LFR models outperform the BLA, the noise levels are not fully met for SNR of 60 dB and 40 dB, most plausibly due to the ZOH discretization.

Performance on test data

We conclude by evaluating the performance of the trained NL-LFR models on unseen test data. The test set is a different random-phase realization of a multisine with the same properties as the training data. Figure 6 presents the simulation results in both time and frequency domains for all noise levels. The nonlinear and noise distortion levels are computed from the training data via the BLA estimation procedure described in [16, Ch. 4.3.1]. The performance is comparable to that on the training data, with time-domain output NRMSEs similar to those in Table 2. In the frequency domain, optimal performance is, indeed, not achieved for SNRs of 60 dB and 40 dB, as the noise level is not met.

The frequency-domain plots provide an additional validation of the BLA approach, as the residual between the measured response and the fitted linear model aligns with the nonparametrically estimated variance estimates. This observation indicates that the BLA captures the full linear contribution of the system dynamics, with the remaining mismatch attributable to nonlinear distortions and measurement noise.

4.2. MDOF mass-spring-damper system

In the previous simulation example, we considered an SDOF system where the nonlinearity depended directly on the measured output. The following simulation study investigates an MDOF system characterized by a nonlinear restoring force dependent on an unmeasured state. Under these conditions, classical RFS approaches are not applicable.

A schematic overview of the MDOF system is shown in Fig. 7. The system comprises two masses, m_1 and m_2 , connected by linear springs and dampers, with the first mass linked to the ground via a nonlinear restoring force. The second mass serves as both the excitation and measurement point. The corresponding physical parameter values are listed in Table 4. Defining $z(t) = [x_1(t), \dot{x}_1(t)]^T$, the nonlinear restoring force is modeled as the sum of a cubic spring

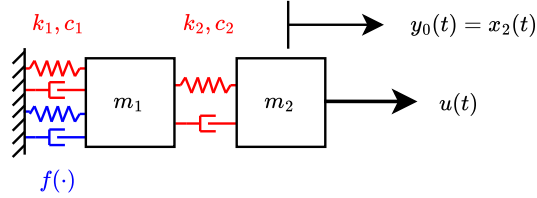


Figure 7: Schematic overview of the MDOF system. We excite and measure at the second mass, but the nonlinearity is between the first mass and the ground, which makes classical RFS approaches inapplicable.

Table 4

True and estimated linear parameters of the MDOF mass-spring-damper system shown in Fig. 7. The value between parentheses indicates the effective linear damping coefficient that takes into account the contribution of the nonlinear damping term around zero velocity.

	m_1 [kg]	m_2 [kg]	c_1 [N s m ⁻¹]	c_2 [N s m ⁻¹]	k_1 [N m ⁻¹]	k_2 [N m ⁻¹]
true	2.00	1.00	5.00 (26.0)	2.00	800	600
estimated	1.97	0.998	24.2	1.97	796	600

and a damper with smooth saturation:

$$f(z(t)) = \alpha_1 \tanh(\alpha_2 z_2(t)) + \alpha_3 z_1^3(t), \quad (27)$$

with parameters $\alpha_1 = 7.0$, $\alpha_2 = 3.0$, and $\alpha_3 = 5.0 \times 10^4$. The corresponding continuous-time state-space matrices in (3) can be obtained directly from the schematic in Fig. 7 and are therefore omitted for brevity.

Synthetic, noiseless input-output data are generated by numerically solving the continuous-time system using the RK4 integration scheme. The training set comprises $R = 6$ realizations, each containing $P = 1$ steady-state period of a random-phase multisine (4), with $N = 8192$ samples per realization. The multisine input signal excites frequencies up to 10 Hz, is sampled at $f_s = 128$ Hz, and its individual amplitudes U_k are chosen to yield an overall RMS amplitude of 10 N. The output is defined as the displacement of the second mass.

The initial values of the linear parameters are defined as

$$\begin{bmatrix} m_{i,0} \\ c_{i,0} \\ k_{i,0} \end{bmatrix} = \begin{bmatrix} m_i(1 + \delta_{m_i}) \\ c_i(1 + \delta_{c_i}) \\ k_i(1 + \delta_{k_i}) \end{bmatrix}, \quad \text{where } \delta_{m_i}, \delta_{c_i}, \delta_{k_i} \sim \mathcal{U}(-0.9, 0.9), \quad (28)$$

for $i \in \{1, 2\}$. We perform 10 optimization runs with a maximum of 100 Levenberg-Marquardt iterations each, starting from different initial guesses, and proceed to the subsequent steps with the best performing model. Next, for the modeling of the restoring force, we use $H = 15$, $N_0 = 100$, and $\lambda = 10^{-8}$ in the nonparametric inference step. An odd polynomial of degree 7, without cross-terms, is then fitted to the inferred data. The results of both steps are shown in Fig. 8.

Remark 7. During the nonparametric inference step, it is not necessary to specify whether the nonlinear restoring force originates from the spring, the damper, or a combination of both. Only the location of the nonlinearity needs to be specified. The precise nature of the nonlinearity can be decided later when fitting the polynomial model. This decision can be guided by visual inspection of a 3D plot such as Fig. 8, or through cross-validation over different candidate input configurations.

In the final optimization step, a maximum of 100 Levenberg-Marquardt iterations is performed with bias regularization parameter $\gamma = 10^{-5}$. The resulting parameter estimates are listed in Table 4. Overall, the estimates are close to the true values, except for the damping coefficient c_1 , which appears to be overestimated by nearly a factor of five. This behavior is, however, expected given the explicit separation of the restoring force into linear and nonlinear components. In particular, the nonlinear saturation term $F_{nl} = \alpha_1 \tanh(\alpha_2 \dot{x}_1)$ in (27) exhibits a non-negligible linear contribution around zero velocity. Linearizing F_{nl} with respect to \dot{x}_1 at $\dot{x}_1 = 0$ yields a slope of 21.0 N s m^{-1} , which,

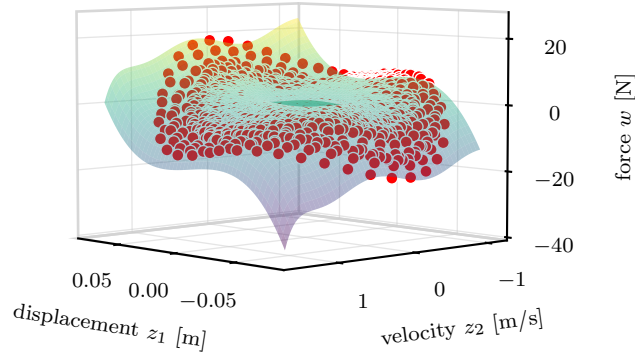


Figure 8: Nonlinear restoring force modeling for the MDOF mass-spring-damper system. The red dots represent the inferred nonparametric samples, while the smooth manifold represents the fitted polynomial model.

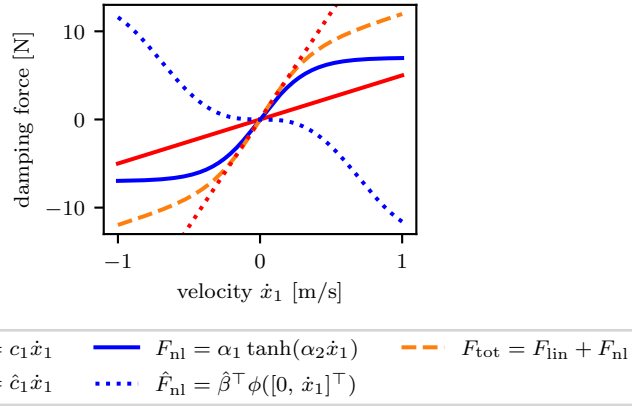


Figure 9: Total damping force decomposed into linear and nonlinear contributions. The apparent overestimation of \hat{c}_1 should be interpreted as the effective linear damping around zero velocity, which includes contributions from both the linear damper and the nonlinear saturation term.

when added to the true linear damping $c_1 = 5.0 \text{ N s m}^{-1}$, results in an effective linear damping of 26.0 N s m^{-1} . This value is significantly closer to the estimated damping coefficient of 24.2 N s m^{-1} . This effect is further illustrated in Fig. 9, which depicts the total damping force F_{tot} as the sum of the linear contribution $F_{\text{lin}} = c_1 \dot{x}_1$ and the nonlinear saturation term $F_{\text{nl}} = \alpha_1 \tanh(\alpha_2 \dot{x}_1)$. The estimated effective linear damping \hat{c}_1 aligns with the tangent of F_{tot} in the low-velocity regime.

We validate the trained NL-LFR models on test data from a multisine realization with the same properties as the training set. Figure 10 shows the simulation results in both the time and frequency domains. The final NL-LFR model achieves an improvement of roughly a factor of ten compared to the BLA model. The figure also includes the initial NL-LFR model from the restoring force modeling step, which already performs close to the final model, indicating that the final optimization mainly serves for bias correction. Further improvement is likely hindered by the ZOH discretization errors discussed previously.

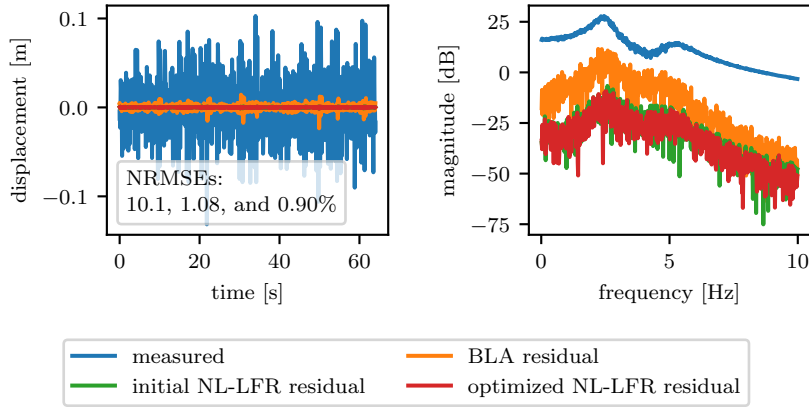


Figure 10: Test data: simulation performance of the MDOF mass-spring damper BLA and NL-LFR models in time and frequency domains. The initial NL-LFR model from the restoring force modeling step already performs close to the final model, which cannot be improved further due to modeling errors originating from the ZOH discretization.

5. Experimental results on the Silverbox benchmark system

The proposed method is evaluated on the experimental data of the Silverbox benchmark [21], which represents an electronic implementation of the Duffing oscillator (24). In this experiment, the input voltage acts as an excitation analogous to mechanical force, whereas the measured output voltage represents the displacement response. The recorded data form an arrow-shaped trajectory consisting of two distinct parts and are sampled at approximately 610 Hz. The first part, referred to as the “arrowhead” and used exclusively for testing, contains 40 000 samples of a white Gaussian noise signal with gradually varying amplitude, filtered using a 9th-order Butterworth filter with cutoff frequency 200 Hz. The remaining data correspond to ten consecutive realizations of a random-phase multisine excitation, together comprising 86 750 samples and exciting only odd harmonics up to 200 Hz. From this multisine portion, the final 21 688 samples are reserved for testing purposes. Successive realizations are separated by short zero-input intervals and slightly exceed one full period length to accommodate transient samples, which are removed prior to analysis to ensure steady-state operation. The data can be considered nearly noise-free [21]; yet, it is not possible to compute the sample noise variance of the output, as each multisine realization consists of only a single period (see Appendix A).

The experimental Silverbox data deviate from ideal identification conditions in two respects. The input signal is measured after passing through a low-pass filter [21], such that it no longer satisfies the ZOH excitation of Assumption 2. Furthermore, the sampling frequency is only about three times higher than the maximum excited frequency. In system identification practice, sampling rates between ten and twenty times the highest frequency of interest are commonly recommended to accurately approximate continuous-time dynamics and to limit discretization errors. The relatively low sampling rate therefore introduces additional modeling inaccuracies. To alleviate these effects, the data are upsampled by a factor of twenty using cubic spline interpolation, after which simulation errors are evaluated on the downsampled signals.

As the Silverbox implements the dynamics of a Duffing oscillator, we assume the model structure in (25). We follow the step-wise procedure using the same optimization settings as in the previous sections. For BLA estimation, the initial values of the linear parameters are taken from [8]. In the sliding-window approach, we use a prediction horizon length of $H = 10$, an offset length $N_0 = 100$, and a regularization strength of $\lambda = 10^{-1}$. The static nonlinearity is modeled using a third-order polynomial, and a bias correction with $\gamma = 10^{-1}$ is applied during the final optimization step. Both optimization steps used a maximum of 100 Levenberg-Marquardt iterations.

Figure 11 presents the simulation results on the arrowhead test data. The left plot shows the time-domain performance of the BLA and NL-LFR models, while the right plot displays the corresponding nonlinear restoring force as simulated by the NL-LFR model, which is clearly cubic. The NL-LFR output simulation error is reduced by more than a factor of sixteen compared to the BLA model. The performance increase is also apparent from Table 5, which shows the simulation errors of both models on both test datasets. It is worth noting that the NL-LFR errors are very consistent, even in the extrapolation region, thanks to the correctly assumed nonlinear structure.

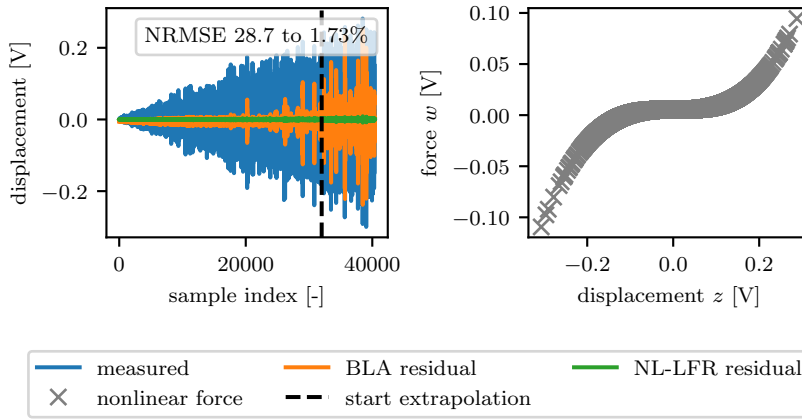


Figure 11: Simulation performance of the BLA and NL-LFR models on the Silverbox arrowhead test data (left), and the corresponding nonlinear restoring force as simulated by the NL-LFR model (right).

Table 5

BLA and NL-LFR simulation errors on the Silverbox test datasets. The NL-LFR model remains accurate even in the extrapolation region of the arrowhead data thanks to its correctly assumed nonlinear structure.

	BLA		NL-LFR	
	NRMSE	RMSE	NRMSE	RMSE
multisine	16.1 %	8.72 mV	1.54 %	0.825 mV
arrowhead (full)	28.7 %	15.3 mV	1.74 %	0.927 mV
arrowhead (no extrapolation)	19.7 %	8.47 mV	1.61 %	0.684 mV

Table 6

BLA and NL-LFR output simulation errors on the Silverbox test datasets when the data are upsampled by only a factor of five instead of twenty. Compared to Table 5, the errors increase significantly, especially for the NL-LFR model, highlighting the importance of proper upsampling.

	BLA		NL-LFR	
	NRMSE	RMSE	NRMSE	RMSE
multisine	16.8 %	9.11 mV	5.25 %	2.85 mV
arrowhead (full)	29.1 %	15.4 mV	5.89 %	3.14 mV
arrowhead (no extrapolation)	20.3 %	8.70 mV	5.30 %	2.28 mV

The results in Table 5 outperform reported results in studies that identify physical model parameters from data, although there are not many physics-based methods to compare with. In [18], a 2.1 mV output RMS error (RMSE) was reported on the arrowhead data, while [8] reports a 2.9 % output NRMSE on a fragment of the multisine data. As all three methods adopt the same model structure, the discrepancies between the proposed method and the results reported in [18] and [8] are likely attributable to differences in the discretization schemes used during optimization. This claim is supported by Table 6, which reports simulation errors on test data when the training data were upsampled by only a factor of five instead of twenty. For the NL-LFR model in particular, the errors increased by more than a factor of three, emphasizing that proper upsampling is essential for simulation performance.

6. Conclusion

This work introduced a novel approach to identifying and modeling the nonlinear restoring force in MDOF systems formulated as NL-LFR state-space models. In contrast to traditional RFS approaches, the proposed method relaxes the measurement assumptions considerably. In particular, any output quantity can be measured (displacement, velocity, or acceleration), only a subset of the degrees of freedom needs to be measured, and the measurements may be noisy.

Starting from an initial linear model, the nonlinear restoring force is reconstructed from measured data using a sliding-window approach. The resulting nonparametric estimate is subsequently used to identify the static nonlinear mapping within the NL-LFR structure by fitting a polynomial basis function model. Since both the nonparametric inference and nonlinear parametrization admit closed-form solutions, the overall identification procedure remains computationally efficient and straightforward to implement. A final optimization stage improves simulation accuracy while compensating for any bias in the estimated physical parameters. Validation on simulated examples and experimental Silverbox data confirms accurate nonlinear model identification, with remaining discrepancies primarily attributed to unavoidable discretization effects.

Although the proposed algorithm relies on periodic multisine data, this requirement mainly supports the frequency-domain estimation of the BLA and the final optimization stage. The central contribution of this work, the sliding-window estimation of the nonlinear restoring force, is not intrinsically tied to periodic data. As a result, extending the method to arbitrary input-output measurements is relatively straightforward by carrying out the remaining estimation steps directly in the time domain.

A. Computing the sample noise covariance

Given $P > 1$, we can compute sample noise covariance matrices that quantify the disturbing noise source $v(n)$. These matrices are useful as they (i) provide insight into the noise properties, (ii) form the basis for defining weighting matrices in the parameter estimation procedure, and (iii) support model validation.

In the time domain, the sample noise covariance matrix is computed as

$$\hat{\Sigma}_y^{\text{time}} = \frac{1}{NR(P-1)} \sum_{n=0}^{N-1} \sum_{r=0}^{R-1} \sum_{p=0}^{P-1} (y^{[r,p]}(n) - y^{[r]}(n))(y^{[r,p]}(n) - y^{[r]}(n))^T, \quad (29)$$

where $y^{[r]}(n) = \frac{1}{P} \sum_{p=0}^{P-1} y^{[r,p]}(n)$ denotes the sample mean over the periods. In the frequency domain, the sample noise covariance matrix at frequency line k is computed as

$$\hat{\Sigma}_y^{\text{freq}}(k) = \frac{1}{R(P-1)} \sum_{r=0}^{R-1} \sum_{p=0}^{P-1} (Y^{[r,p]}(k) - Y^{[r]}(k))(Y^{[r,p]}(k) - Y^{[r]}(k))^H, \quad (30)$$

where $Y^{[r]}(k) = \frac{1}{P} \sum_{p=0}^{P-1} Y^{[r,p]}(k)$ denotes the sample mean over the periods. Note that in the time domain, we average over all samples as the noise is assumed stationary, whereas in the frequency domain, each frequency is treated separately since the noise may be frequency-dependent.

CRedit authorship contribution statement

Merijn Floren: Conceptualization, Formal analysis, Methodology, Software, Validation, Visualization, Writing – original draft preparation. **Jan Swevers:** Funding acquisition, Resources, Supervision, Writing – review and editing.

Declaration of Generative AI and AI-assisted technologies in the writing process

During the preparation of this work, the authors used ChatGPT to assist with language refinement, grammatical corrections, and improvements to clarity and conciseness of the manuscript text. After using this tool, the authors reviewed and edited all content as needed and take full responsibility for the content of the publication.

References

- [1] Bonisoli, E., Vigliani, A., 2007. Identification techniques applied to a passive elasto-magnetic suspension. *Mechanical Systems and Signal Processing* 21, 1479–1488.
- [2] Bradbury, J., Frostig, R., Hawkins, P., Johnson, M.J., Leary, C., Maclaurin, D., Necula, G., Paszke, A., VanderPlas, J., Wanderman-Milne, S., Zhang, Q., 2018. JAX: composable transformations of Python+NumPy programs. URL: <http://github.com/google/jax>. software available from <http://github.com/google/jax>.
- [3] Dossogne, T., Noel, J.P., Kerschen, G., Peeters, B., Debille, J., Vaes, M., Schoukens, J., 2015. Nonlinear ground vibration identification of an F-16 aircraft. Part II: Understanding nonlinear behaviour in aerospace structures using sine-sweep testing, in: *International Forum of Aeroelasticity and Structural Design (IFASD)*, pp. 751–769.

- [4] Enqvist, M., Ljung, L., 2005. Linear approximations of nonlinear FIR systems for separable input processes. *Automatica* 41, 459–473.
- [5] Floren, M., Noël, J.P., 2022. Nonlinear restoring force modelling using Gaussian processes and model predictive control, in: *Conference Proceedings of ISMA2022-USD2022*, pp. 2493–2498.
- [6] Göge, D., Sinapius, J.M., 2006. Experiences with dynamic load simulation by means of modal forces in the presence of structural nonlinearities. *Aerospace Science and Technology* 10, 411–419.
- [7] Kidger, P., Garcia, C., 2021. Equinox: neural networks in JAX via callable PyTrees and filtered transformations. *Differentiable Programming workshop at Neural Information Processing Systems 2021*.
- [8] Kocijan, J., 2018. Parameter estimation of a nonlinear benchmark system. *Science, Engineering & Education* 1, 3–10.
- [9] Levenberg, K., 1944. A method for the solution of certain non-linear problems in least squares. *Quarterly of Applied Mathematics* 2, 164–168.
- [10] Marquardt, D.W., 1963. An algorithm for least-squares estimation of nonlinear parameters. *Journal of the Society for Industrial and Applied Mathematics* 11, 431–441.
- [11] Masri, S., Bekey, G., Sassi, H., Caughey, T., 1982a. Non-parametric identification of a class of nonlinear multidegree dynamic systems. *Earthquake Engineering & Structural Dynamics* 10, 1–30.
- [12] Masri, S., Caughey, T., 1979. A nonparametric identification technique for nonlinear dynamic problems. *Journal of Applied Mechanics* 46, 433–447.
- [13] Masri, S., Chassiakos, A., Caughey, T., 1993. Identification of nonlinear dynamic systems using neural networks. *Journal of Applied Mechanics* 60, 123–133.
- [14] Masri, S., Sassi, H., Caughey, T., 1982b. Nonparametric identification of nearly arbitrary nonlinear systems. *Journal of Applied Mechanics* 49, 619–628.
- [15] Noël, J.P., Kerschen, G., 2017. Nonlinear system identification in structural dynamics: 10 more years of progress. *Mechanical Systems and Signal Processing* 83, 2–35.
- [16] Pintelon, R., Schoukens, J., 2012. *System Identification: A Frequency Domain Approach*. 2nd ed., John Wiley & Sons, Hoboken, NJ.
- [17] Rader, J., Lyons, T., Kidger, P., 2024. Optimistix: modular optimisation in JAX and Equinox. [arXiv:2402.09983](https://arxiv.org/abs/2402.09983).
- [18] Rogers, T.J., Friis, T., 2022. A latent restoring force approach to nonlinear system identification. *Mechanical Systems and Signal Processing* 180, 109426.
- [19] Saad, P., Al Majid, A., Thouverez, F., Dufour, R., 2006. Equivalent rheological and restoring force models for predicting the harmonic response of elastomer specimens. *Journal of Sound and Vibration* 290, 619–639.
- [20] Van Loan, C., 2003. Computing integrals involving the matrix exponential. *IEEE Transactions on Automatic Control* 23, 395–404.
- [21] Wigren, T., Schoukens, J., 2013. Three free data sets for development and benchmarking in nonlinear system identification, in: *2013 European Control Conference (ECC)*, IEEE, pp. 2933–2938.
- [22] Worden, K., 1990. Data processing and experiment design for the restoring force surface method, part I: integration and differentiation of measured time data. *Mechanical Systems and Signal Processing* 4, 295–319.